View metadata, citation and similar papers at core.ac.uk
brought to you by CORE
provided by NASA Technical Reports Server

Preliminary Design of the Superconducting Rotor for NASA's High-Efficiency Megawatt Motor

Dr. Justin J. Scheidler*
NASA Glenn Research Center, Cleveland, Ohio, 44135

NASA Glenn Research Center is developing a 1.4 MW high-efficiency electric machine for future electrified aircraft to reduce energy consumption, emissions, and noise. This wound-field, synchronous machine employs a self-cooled, superconducting rotor to achieve excellent specific power and efficiency. The design of the superconducting rotor and the optimization of its electromagnetic and structural responses are analyzed in this paper. Candidate designs are evaluated in terms of absolute performance, specific performance, and performance per cost. It is found that optimizing the electromagnetic response for absolute or specific performance yields designs that are similar to each other, but opposite of the cost-optimized design. A method to define the thermal requirements of the superconducting coils and integrated cryocooler is also presented.

Introduction

To drastically reduce the energy consumption, emissions, and noise of future commercial transport aircraft, NASA is investing in a broad portfolio of enabling research and development for electrified aircraft propulsion (EAP) [1]. A number of transport aircraft concepts that harness EAP have been shown to provide system-level benefits to energy consumption, fuel burn, and/or emissions [2–8]. As expected, the existence of the benefits and their magnitude depend on the assumed performance of the individual EAP components. Two of the more influential characteristics are the specific power and efficiency of the EAP system's electric machines. Specific power several times greater than industrial motors and efficiency at or above the state of the art (96%) are typically needed for an aircraft concept to be promising. Accordingly, NASA's EAP investment includes the development of three megawatt-class electric machines that each combine high specific power (>13 kW/kg) with high efficiency (>96%) [1]. For transport aircraft up to the single-aisle class, a megawatt-level continuous power rating permits the use of several different EAP configurations (e.g., parallel hybrid, partially turboelectric, or fully turboelectric).

The most forward reaching of the three aforementioned electric machines is the 1.4 MW wound-field synchronous machine being developed at NASA Glenn Research Center. The machine is referred to as the High Efficiency Megawatt Motor (HEMM). The key performance goals and characteristics of the HEMM are summarized in Table 1. To illustrate the effect of this machine on a transport aircraft with EAP, system-level studies have been performed for one concept aircraft, the NASA single-aisle turboelectric aircraft with aft boundary layer propulsor (STARC-ABL). Relative to the baseline STARC-ABL configuration, the electric machine performance targets established by NASA (13 kW/kg, 96%) provide a 7% to 10% reduction in fuel burn [7]. Compared to this benefit of NASA's performance targets, the more stringent goals of HEMM (16 kW/kg, 98% to 99%) provide an additional 1.5% to 2.5% reduction in fuel burn, respectively [1]. It should be noted that further refinements to the analyses in [7] (and referenced in [1]) are currently being conducted and updated results are expected soon. A potentially more impactful benefit is that such an increase in efficiency to 98% or 99% will reduce the amount of waste heat that must be managed by a factor of 2 to 4, respectively.

Table 1 Key characteristics and performance goals of NASA Glenn's electric machine for EAP systems.

Continuous power rating, MW	Motor type	Speed, rpm	Specific power goal, kW/kg	Efficiency goal, %
1.4	Wound field synchronous	6,800	16	>98

The exceptional specific power and efficiency of the HEMM is primarily achieved by utilizing a slotless stator and a

*Research Mechanical Engineer, Rotating and Drive Systems Branch, 21000 Brookpark Road, Cleveland, Ohio, 44135.

self-cooled, superconducting rotor. A superconducting field winding has a negligible amount of internal energy loss* and can produce magnetic field strengths that greatly exceed those produced by conventional conductors or permanent magnets. However, the use of superconductors introduces a number of challenges. Superconductors must be kept at cryogenic temperatures and the superconducting system must be carefully designed to avoid a loss of superconductivity, which will occur when the temperature, magnetic flux density, or conduction current in the superconductor exceed design limits. Additionally, superconductors are fragile compared to copper and aluminum conductors; superconductors are subject to maximum strain and minimum bend radius constraints, and care must be taken to avoid appreciable shear stresses and transverse tensile stresses. When utilized in a rotor, the aforementioned challenges impose considerable risk. Superconductors are also significantly more expensive than copper and aluminum conductors. Consequently, it is important to conduct analysis and sub-scale testing prior to full-scale implementation to overcome these risks.

This paper details the preliminary design of the superconducting rotor for NASA's HEMM. The electromagnetic and structural analyses are presented as well as the optimization of its electromagnetic response. The benefits and drawbacks of candidate designs are discussed. The preliminary design is evaluated in terms of absolute performance, specific performance (i.e., performance per mass), and performance per cost. Although the thermal analysis is not included in this paper, a method to define the thermal requirements of the superconducting coils and integrated cryocooler is described.

Electromagnetic design and optimization

The pertinent characteristics and fixed geometric parameters of the HEMM are summarized in Table 2.

Table 2 Characteristics and fixed geometric parameters of NASA's HEMM; see Fig. 2 for the definition of the rotor coil gaps.

Characteristic/parameter	Value	Characteristic/parameter	Value
Rotation speed, rpm	6,800	Superconductor width, mm	4
Electrical frequency, Hz	DC	Superconductor thickness, μm	65
Number of poles	12	Min. superconductor bend radius, mm	15
Stator configuration	slotless	Max. magnetic flux density in the superconductor, T	2
Stator outside diameter, cm	37.5	Rotor coil gap g_1, mm	1.3
Stator inside diameter, cm	34	Rotor coil gap g_2, mm	1.0
Rotor outside diameter, cm	30	Rotor coil gap g_3, mm	1.3
Rotor inside diameter, cm	20.5	Rotor coil gap g_4, mm	1.3
Rotor/stator axial length, cm	12.5		

A 2nd generation high temperature superconductor (REBCO: rare Earth-barium-copper-oxide) was selected over other superconductors, because they are commercially available in long piece lengths and can provide sufficient performance at high temperatures (about 77 K and below) in moderately strong magnetic environments. The 2nd generation high temperature superconductors (2G HTS) are available in a variety of widths and thicknesses (depending on the thickness of non-superconducting encapuslation that is needed). A conventional non-superconducting winding, or coil, requires that each turn in the coil is electrically insulated from the other turns. This limitation does not apply to most superconducting coils that carry DC currents or AC currents of sufficiently low frequency; even without turn-to-turn insulation, the applied current prefers to flow in the turns of superconductor rather than short from turn to turn through the superconductor's resistive sheath. Such no insulation (NI) superconducting coils were introduced in 2011 [9]. Compared to insulated superconducting coils, NI superconducting coils have several benefits, including higher engineering current density (or smaller size), better mechanical strength, fault tolerance (immunity to quench, i.e., a loss of superconductivity) [10], and resistance to conductor defects [11]. For these reasons, NI superconducting coils were chosen. This selection allows the superconductor's thickness to be reduced to 65 μm (from the typical

*Not including the conventional conductors that supply the superconductor with current from room temperature, a superconducting winding only exhibits loss due to the resistive splice joints between superconductor segments and AC losses caused by alternating conduction current and/or alternating external magnetic flux.

100 μm), which enables a given coil design to have a 54% higher magnetomotive force. At the stage of the design presented here, an extra 10 μm was allocated to each turn of the coil to account for the possible inclusion of a co-wound electrically-conductive material (e.g., metal tape or thermal grease).

Thermal requirements of the superconducting coils

This section will present a method to define the thermal requirements of the superconducting coils and integrated cryocooler. The method is based on a collection of measurements from the manufacturer and two de-rating factors. The result of the method is a curve that defines the approximate maximum temperature in the superconductor for a given DC current.

Although the selected NI superconducting coil configuration is fault tolerant and should not be permanently damaged by a loss of superconductivity, superconductor quench is still undesirable, because it is possible that a coil fabrication defect or stress transient during operation will eliminate the protection capability (i.e., turn-to-turn contact) in a small region of the coil. Also, quench will result in temporary heat generation within the coil that must be conducted out to the cryocooler.

The critical current of a 2G HTS depends on the orientation of the applied magnetic flux density. Due to this angular dependence, the design current must be calculated for the worst case condition (i.e., the orientation that provides the minimum critical current). Hence, the datasheet values of critical current, which are defined at only 2 specific angles by convention, must be de-rated to account for the angular dependence of the critical current. Here, an additional de-rating factor of -35%, or a safety factor of about 1.5, is applied to account for modeling inaccuracy and the variability of manufactured conductor.

As indicated in Table 2, the magnetic flux density in the 4 mm wide superconductor will be limited to 2 T. For this condition, Table 3 summarizes the critical current (nominal and de-rated for angular dependence) of a high performance tape from the manufacturer's data. It can be seen that considering the angular dependence reduces the allowable critical current by 22 % to 32 %. Data for a standard performance tape, which will be used in the HEMM, was not available. Thus, its nominal critical current was calculated using the measured lift factor of the high performance tape and the critical current of the standard performance tape at self field (s.f.) and 77 K. The design (allowable) current of the standard performance tape is calculated by applying the -35% de-rating to the right most column of Table 3 followed by a quadratic interpolation. The result is shown in Fig. 1, where any point on the curve is a valid operating point. Higher current is desired to increase the torque (and thus specific power) of HEMM, but the reduced temperature limit imposes stricter requirements on the cryoooler and thermal design. A design current of 51.5 A and temperature limit of 62.8 K was selected to balance these aspects.

Table 3 Critical current I_c (nominal and de-rated for angular dependence) and lift factor $LF = I_c\,(T)\,/I_c\,(77\text{K})$ of a high performance 2G HTS from the manufacturer's data and the calculated critical currents of a standard performance 2G HTS.

Temp., K	High performance tape (191 A at s.f., 77 K)			Standard tape (150 A at s.f., 77 K) (calculated)	
	nominal I_c, A	min[$I_c\,(\theta)$], A	$LF\,(0^o)$, –	nominal I_c, A	min[$I_c\,(\theta)$], A
50	249.4	193.7	1.33	199.5	155.0
65	127.1	86.3	0.67	99.9	67.8
77	28.9	21.0	0.15	22.7	16.5

Optimization of the rotor coil's geometry

Several geometric parameters of the rotor can be varied as shown in Fig. 2, such as the geometry and location of the coils, the width of the rotor teeth, and the minimum thickness of the rotor's soft magnetic material. For an allotted volume of superconductor, the machine's performance will be maximized if the magnetomotive force of the rotor coils is maximized. Therefore, the rotor's geometry can be optimized for electromagnetic performance in two steps. First, the magnetomotive force of each rotor coil is optimized for a given geometry of the soft magnetic material by maximizing the number of turns in each coil. Second, the geometry of the soft magnetic material is optimized. This section discusses the first step in this optimization process. The subsequent section discusses the second step in the process.

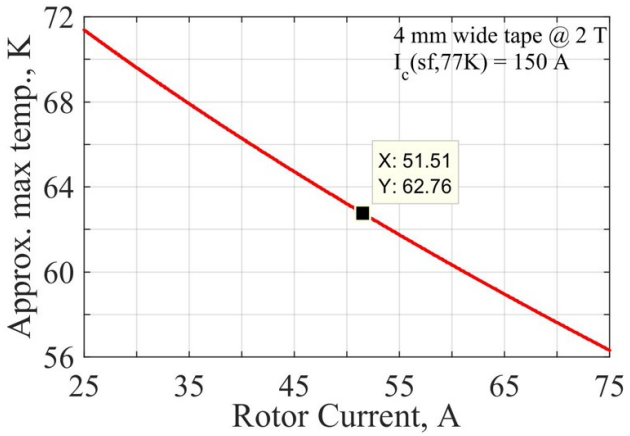

Fig. 1 Approximate maximum temperature in the high temperature superconductor as a function of the DC rotor current, including a 1.5 safety factor and accounting for the angular dependence of the conductor's critical current; the chosen operating point (51.5 A current) is indicated.

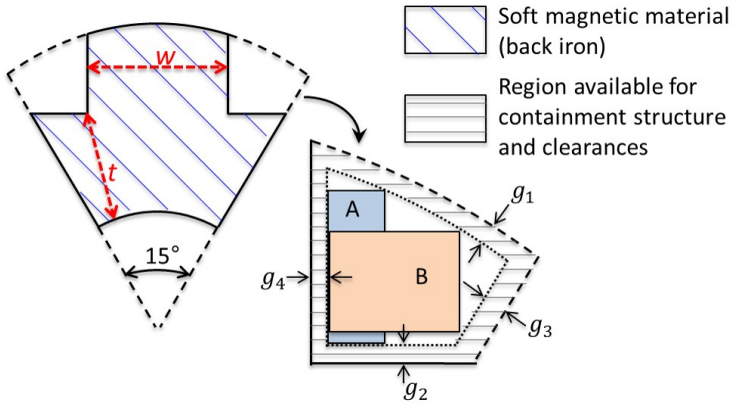

Fig. 2 Possible cross-sectional geometries A and B of the rotor coil for a given choice of the soft magnetic material's geometric parameters (the rotor tooth width, w, and thickness, t) and the rotor coil gaps g_1 through g_4.

As shown in Fig. 2, the available cross-sectional area of each rotor coil is reduced on all sides to account for mechanical clearances and the non-magnetic structure that contains the coil during rotation. Within that reduced area, many rectangular cross sections are possible, each with a different maximum number of turns. The cross section of each coil is optimized for maximum number of turns using a simplex search method. The number of layers in the coil was constrained to be either 1 or even so that both current leads could be located on the same side of the coil (i.e., both inside or both outside).

The results of the optimization are given in Figs. 3 and 4. In Fig. 3b, the mass includes the coils and the soft magnetic material in the rotor and stator. As the width of the soft magnetic material reduces, the number of turns in the coil and the magnetomotive force per mass gradually increase. Since the coil must have an even integer number of layers, reductions in the soft magnetic material's thickness affect the mass but have no effect on the optimal number of turns until there is a step change in the number of layers. The total length of superconductor for each coil exceeds 300 m in some cases. Although it is difficult to procure continuous pieces of 2G HTS at this length, that issue is not a concern here, because the coil is composed of layers of racetrack coils so that only each racetrack coil needs to be wound from a continuous piece. The required length for each racetrack coil is less than 100 m, which is commonly available. This analysis suggests that the coil's performance is maximized when the width and thickness of the soft magnetic material are minimized. However, this analysis neglects the magnetic response of the system. In practice, less soft magnetic material and larger coils will lead to more saturation in the magnetic material and higher magnetic flux densities in the

coils, both of which are detrimental. The finite element analysis in the following section incorporates these constraints.

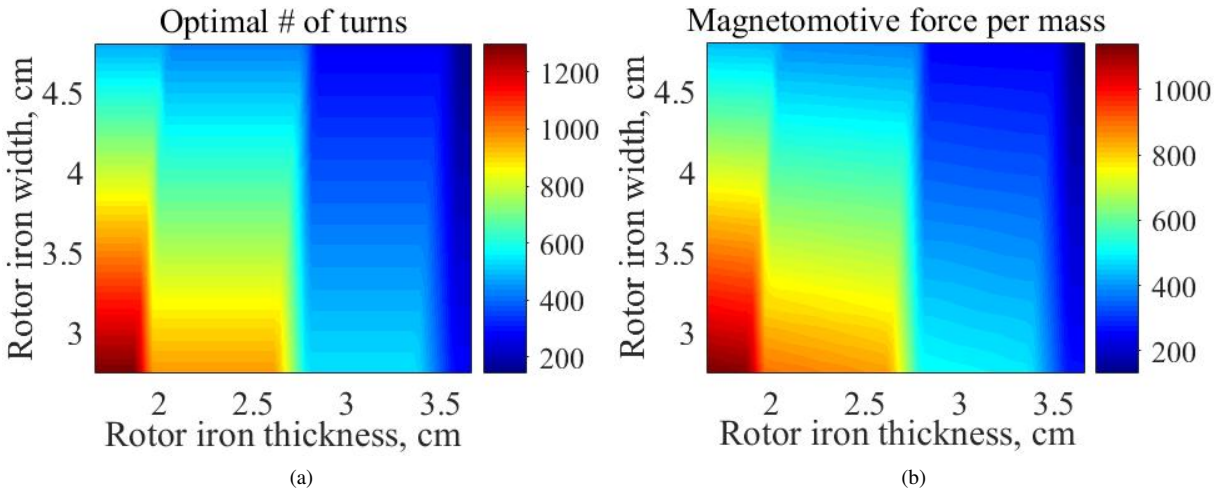

Fig. 3 (a) optimal number of turns in each rotor coil and (b) magnetomotive force per mass (A-turns/kg) for different soft magnetic material geometries.

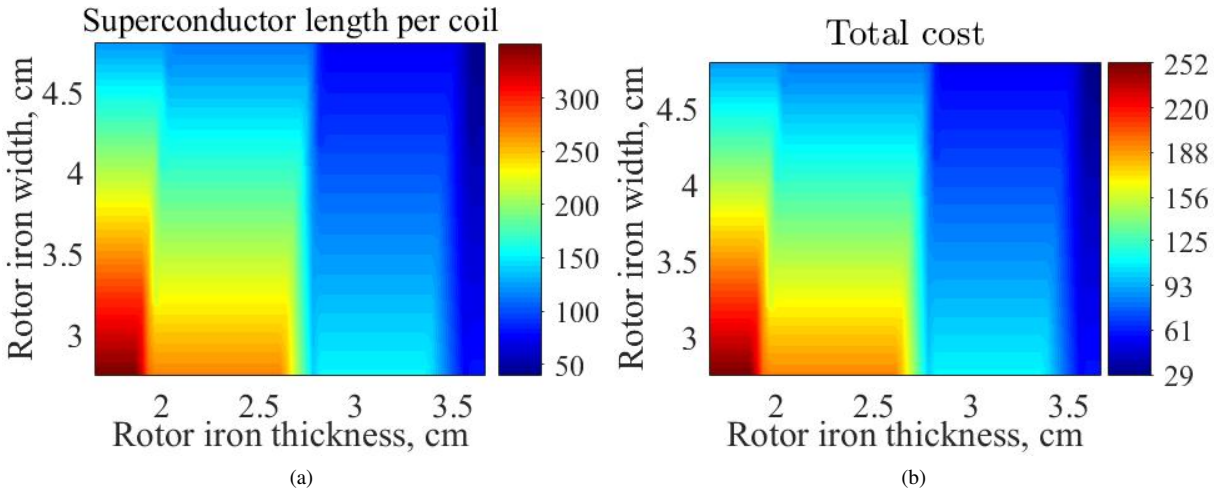

Fig. 4 (a) required length of superconductor (m) in each rotor coil and (b) total cost ($K) of the superconductor in the HEMM (assuming $60/m superconductor cost) for different soft magnetic material geometries.

Magnetostatic finite element analysis

This section describes the 2D and 3D nonlinear, magnetostatic finite element analysis that was conducted to optimize the electromagnetic performance of the superconducting rotor coils. The 2D model is used to explore the entire design space, whereas the 3D model is evaluated in the vicinity of the optimal design.

Due to the use of superconductors, the soft magnetic material in both the rotor and stator can be excited far into magnetic saturation, well outside the range of the manufacturer's data. In this case, simple linear extrapolation can result in significant errors. To considerably improve the accuracy of these simulations, the constitutive response of the soft magnetic material was extrapolated using an updated version of the method in [12] that will be presented in a future publication. The superconducting rotor coils dominate the magnetic response, because their magnetomotive force is about 70 times greater than that of each stator coil. Thus, for this preliminary analysis, the stator coils (and current) are neglected. As a result, only half of a rotor pole needs to be simulated due to symmetry.

For HEMM, the rotor winding produces the magnetic flux that interacts with the stator current to generate the torque. Consequently, the rotor-produced magnetic flux density at the inner diameter of the stator is used as a performance metric for rotor geometry optimization. The candidate designs are evaluated in terms of absolute performance, specific performance (i.e., performance per mass), and performance per cost.

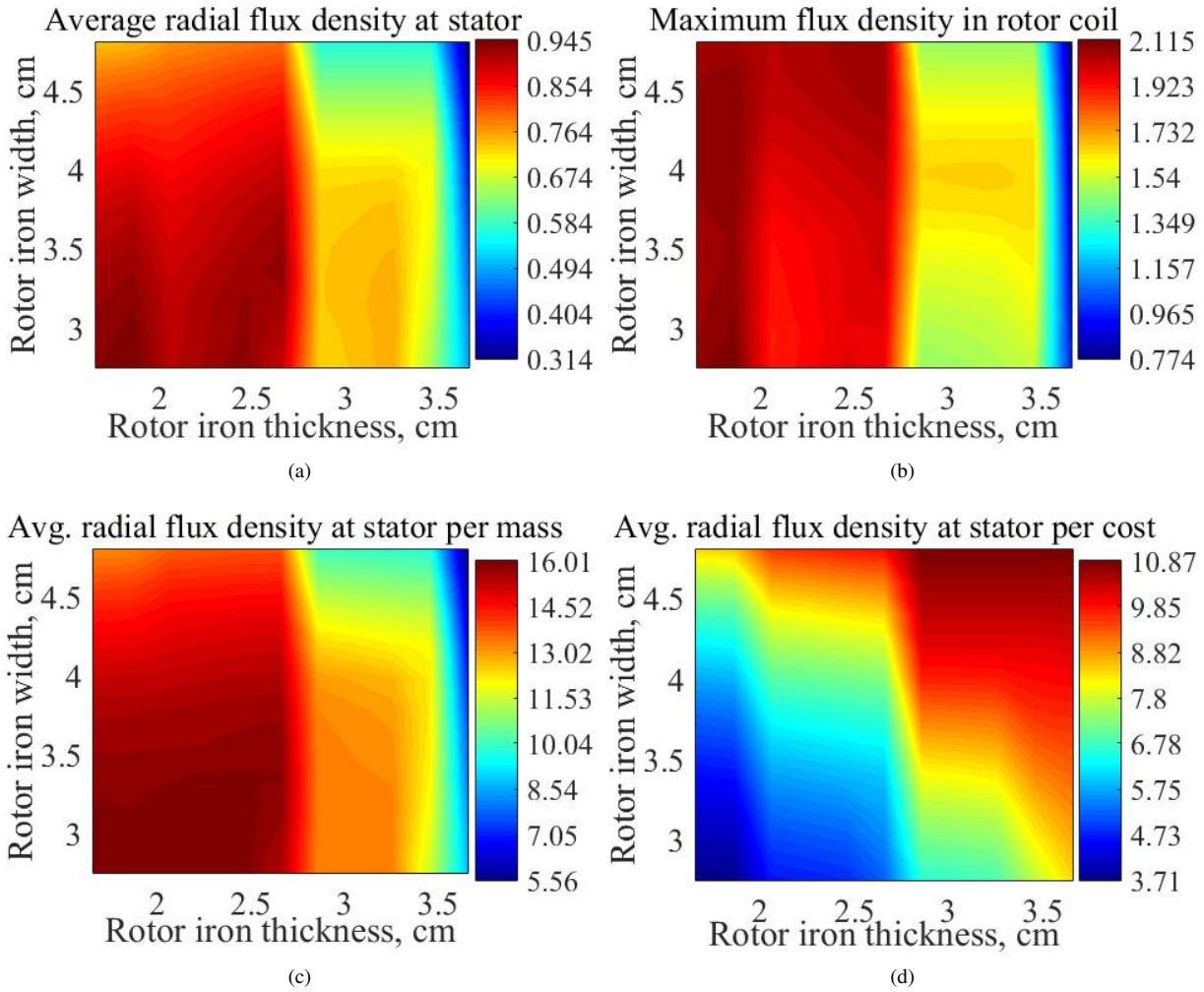

Fig. 5 2D magnetostatic nonlinear finite element results: (a) average radial magnetic flux density (T) at the inner diameter of the stator soft magnetic material, (b) maximum magnetic flux density magnitude (T) in the superconducting coil, (c) average radial magnetic flux density at the inner diameter of the stator soft magnetic material per mass (mT/kg), and (d) average radial magnetic flux density at the inner diameter of the stator soft magnetic material per cost (mT/$1000).

The parametric study results for the 2D model are shown in Fig. 5. The performance and specific performance follow the trends in Fig. 3, but are missing the step change around a soft magnetic material thickness of 2 cm due to magnetic saturation. Alternatively, the performance per cost has the opposite trend, indicating that increases in performance come at a greater and greater cost; this is also a result of magnetic saturation. As more and more of the rotor's soft magnetic material becomes saturated, the coils become less effective at pushing magnetic flux across the large air gap to the stator's soft magnetic material. The maximum magnetic flux density in the coil follows a trend that is similar to the performance metric. In most cases, increases in performance come at the expense of increases in flux density in the coil. However, for thicknesses between about 2 cm and 2.75 cm, both higher performance and lower flux density in the coil can be achieved by reducing the width of the rotor's soft magnetic material. The design current was derived for a flux density limit of 2 T in the coil. Hence, combinations of width and thickness with a max coil flux

density exceeding that limit are invalid operating points.

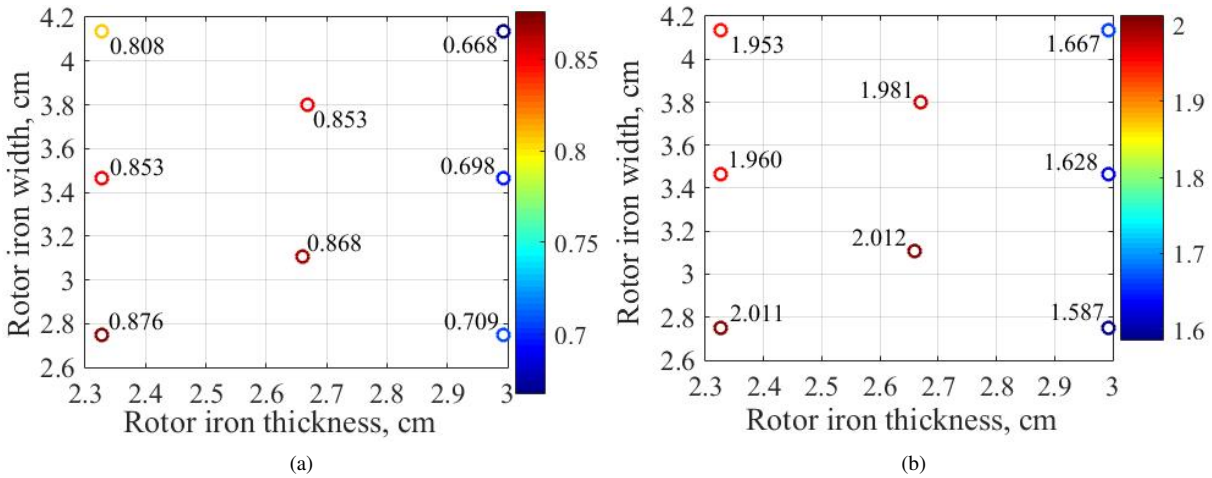

Fig. 6 3D magnetostatic nonlinear finite element results: (a) average radial magnetic flux density (T) at the inner diameter of the stator soft magnetic material, (b) maximum magnetic flux density magnitude (T) in the superconducting coil.

The parametric study results for the 3D model are shown in Fig. 6. Each 3D simulation took about 2 orders of magnitude longer to solve. Thus, only eight 3D simulations were run to understand the change in response from 2D to 3D. Relative to the 2D response, the performance of the 3D simulation is about 7% lower in each case. This level of performance reduction is not unreasonable given that the length-to-diameter aspect ratio of the HEMM is relatively low (0.39, calculated at the middle of the air gap). Unfortunately, the maximum flux density in the coil does not exhibit a corresponding reduction; rather, it has a similar value to the 2D results.

The preliminary design of the magnetic system was selected to maximize performance and specific performance while staying within the coil flux density constraint. Accordingly, a rotor geometry with a thickness of 2.6 cm and width of 3.3 cm was selected.

Rotor containment design and stress analysis

This section presents the stress analysis of the rotor and its containment structure, or winding fixture. This preliminary design only considers the centrifugal loading. The rotor is also subjected to magnetic forces that pull each rotor pole toward the stator, magnetostrictive forces, electromagnetic forces (i.e., the torsion), and thermal contraction forces. In the candidate designs, the magnetomotive force of each rotor coil is about 50 to 100 times greater than that of each stator coil. Since HEMM's stator is slotless, the magnetic flux density in the rotor is effectively constant and the magnetostriction (and magnetostrictive forces) in the rotor are negligible. The magnetic forces that pull each rotor pole toward the stator are neglected, because, in theory, they are balanced such that the net force on the rotor is zero. The thermal contraction forces strongly depend on the specific geometry and material of each rotor component and how the components are in contact with each other. Further, the thermal contraction forces are expected to be relatively small. Thus, the thermal contraction forces are neglected at this stage of the design process. The electromagnetic forces should be primarily applied to the soft magnetic material rather than the superconducting coils, which are the critical component. Hence, the electromagnetic forces are also neglected in this preliminary design.

Rather than iterating between the mechanical and magnetic studies to arrive at a jointly optimal design, an attempt was made to design a containment structure for the optimal magnetic design. Due to the very limited cross-sectional area available for the structure, this was a significant challenge despite the relatively low tip speed of the rotor (107 m/s). Several candidate designs had negative stress margins; some of these invalid designs are shown in Fig. 7. The preliminary design that had positive stress margins is shown in Fig. 8. Each superconducting rotor coil is enclosed within a fixture that has an L-shaped cross section and follows the perimeter of the coil. The coil and fixture are contained by a shoulder on each rotor tooth. Due to the presence of the shoulder, the coils cannot be assembled onto a single-piece rotor. Therefore, each rotor tooth is a separate part that connects through a double dovetail to the ring-shaped portion of the

soft magnetic material. The assembly procedure for one rotor pole is depicted in Fig. 9.

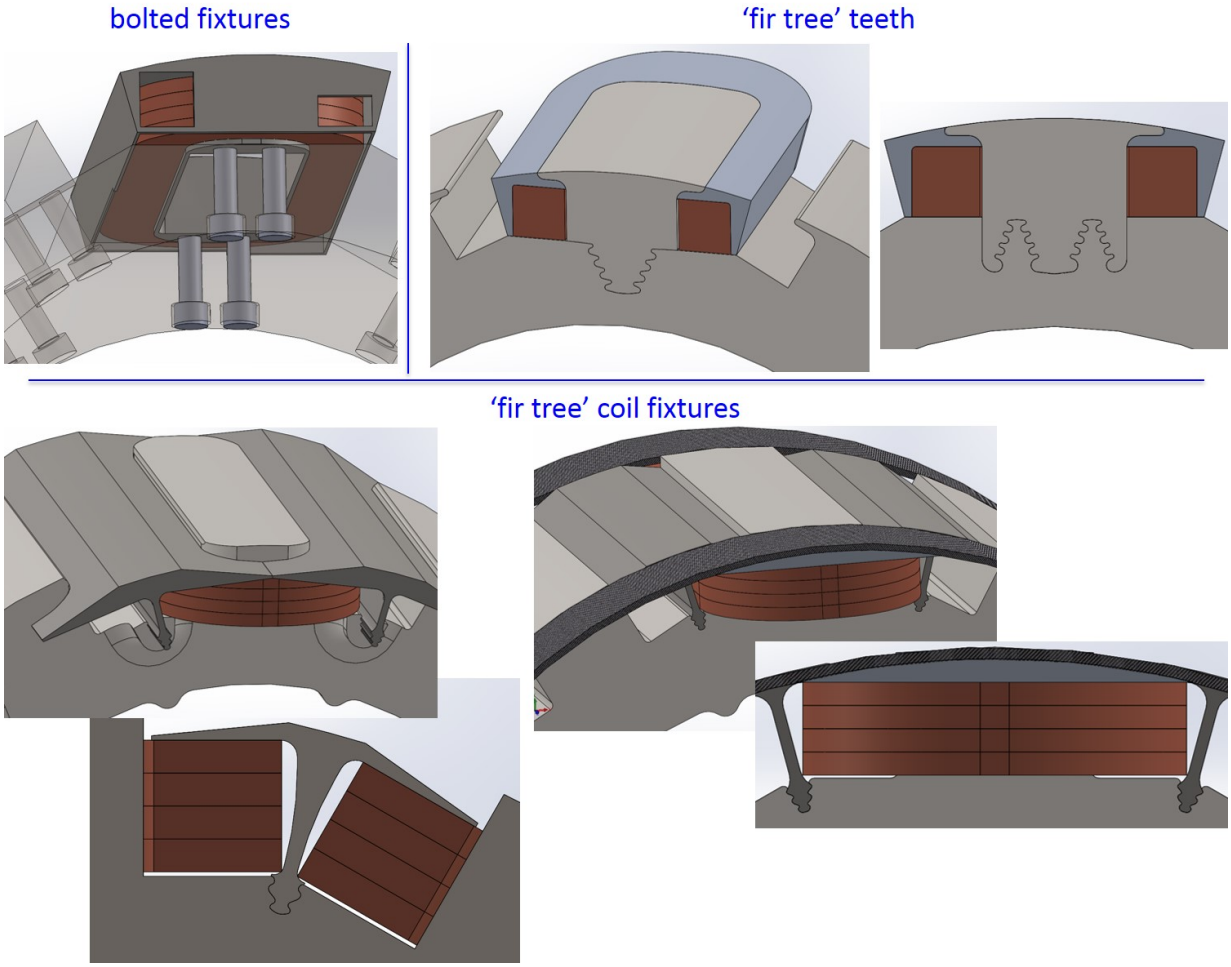

Fig. 7 Candidate designs of the superconducting rotor that had negative stress margins.

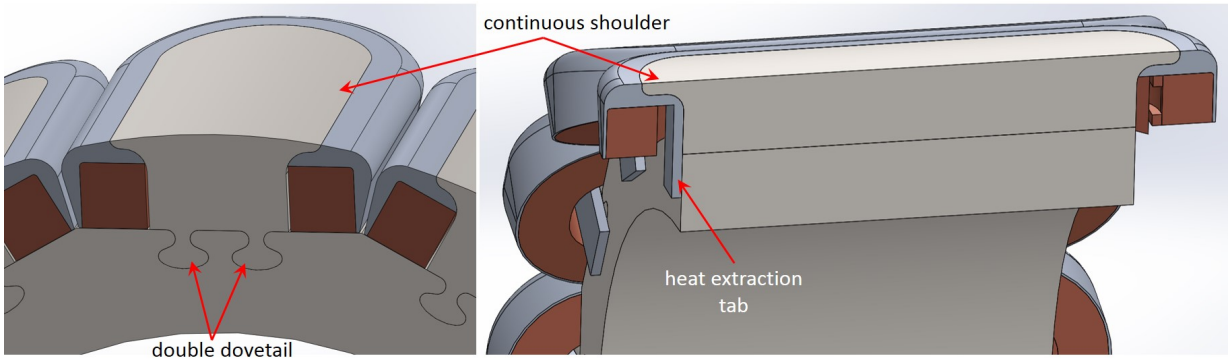

Fig. 8 Preliminary design of the superconducting rotor.

The results of the stress analysis are summarized in Fig. 10 and Table 4. The peak stress in the soft magnetic material is in the fillet between the shoulder and the tooth. To keep this stress within strength limits, the axial length of the rotor's soft magnetic material had to be lengthened by 7 mm on each axial face. This appreciably increased the

mass of the rotor. Several materials with high specific strength were evaluated for the winding fixture. As shown in Table 4, 4 materials (2 ceramics, 1 metal-ceramic composite, and 1 metal) are valid options. The yield strength of the soft magnetic material near the cryogenic operating temperature was estimated from measurement by [13] and the manufacturer's room temperature properties.

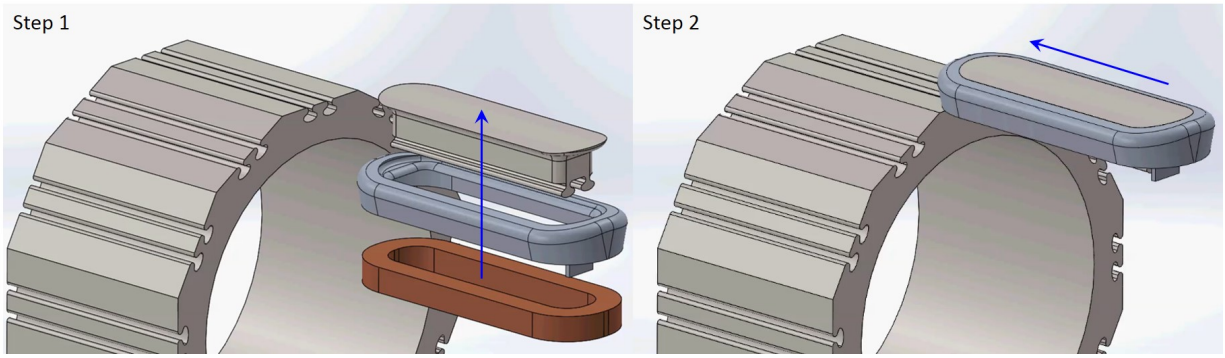

Fig. 9 Assembly procedure for one rotor tooth sub-assembly.

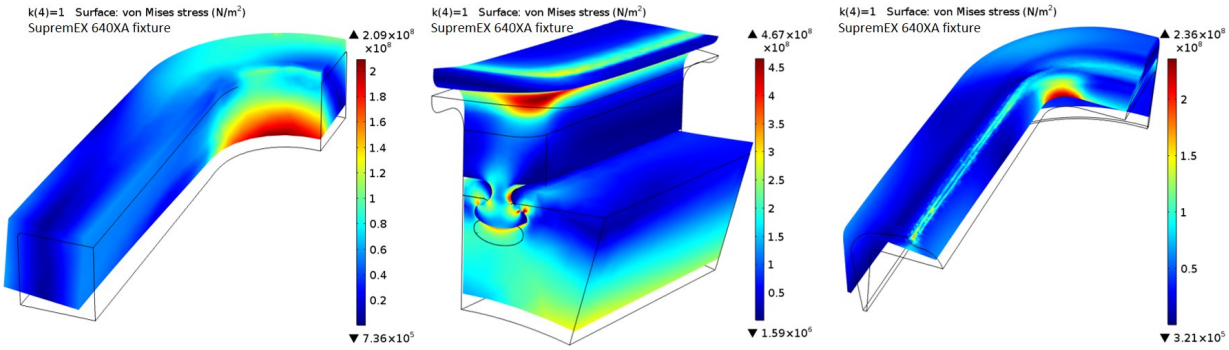

Fig. 10 Example stress analysis results for the preliminary design of the superconducting rotor (electromagnetic forces and thermal contraction neglected).

Table 4 Stress analysis results for the preliminary design of the superconducting rotor (electromagnetic forces and thermal contraction neglected).

Fixture material	Superconductor			Hiperco 50A			Fixture		
	'Failure' strength, MPa	Max von Mises stress, MPa	Margin	'Failure' strength, MPa	Max von Mises stress, MPa	Margin	'Failure' strength, MPa	Max von Mises stress, MPa	Margin
SiC	>550	183	2.01	694 (at 77 K, est.)	480	0.45	550	462	0.19
Sialon ($SiN + Al_2O_3$)		191	1.88		483	0.44	760	391	0.94
SupremEX 640XA (Al 6061 + SiC powder)		209	1.63		467	0.49	560	236	1.37
Ti-6Al-6V-2Sn		239	1.30		516	0.34	1210	338	2.58

Conclusion

This paper detailed the preliminary design of the superconducting rotor for NASA's High Efficiency Megawatt Motor (HEMM), a 1.4 MW partially superconducting wound field machine. A method was presented to define the thermal requirements of the superconducting coils and integrated cryocooler based on the measurements of the superconductor's critical current at different temperatures and magnetic flux orientations. For a given cross-sectional geometry of the rotor's soft magnetic material, the cross-section of each rotor coil was optimized to maximize its magnetomotive force. Then, a near optimal cross-sectional geometry of the rotor's soft magnetic material was identified using a parametric study of 2D and 3D nonlinear magnetostatic finite element models. A structural analysis was conducted to design the mechanical system to react the centrifugal loading with a very geometrically-constrained containment structure. The preliminary design was evaluated in terms of absolute performance, specific performance (i.e., performance per mass), and performance per cost. A containment structure with positive stress margins was designed that enables the optimal magnetic system.

Acknowledgments

This work was sponsored by the NASA Advanced Air Transport Technology Project within the Advanced Air Vehicles Program of NASA's Aeronautics Research Mission Directorate.

References

[1] Jansen, R., Bowman, C., Jankovsky, A., Dyson, R., and Felder, J., "Overview of NASA Electrified Aircraft Propulsion (EAP) Research for Large Subsonic Transports," *53rd AIAA/SAE/ASEE Joint Propulsion Conference, AIAA Propulsion and Energy Forum, Atlanta, GA, AIAA 2017-4701*, 2017. doi:10.2514/6.2017-4701.

[2] Bradley, M. K., and Droney, C. K., "Subsonic Ultra Green Aircraft Research: Phase I Final Report," NASA Contractor Report, NASA/CR-2011-216847, 2011. URL https://ntrs.nasa.gov/search.jsp?R=20110011321&hterms=NASA%2fCR-2011-216847&qs=N%3D0%26Ntk%3DAll%26Ntt%3DNASA%252FCR-2011-216847%26Ntx%3Dmode%2520matchallpartial.

[3] Felder, J. L., Brown, G. V., DaeKim, H., and Chu, J., "Turboelectric Distributed Propulsion in a Hybrid Wing Body Aircraft," *20th International Society for Airbreathing Engines, ISABE-2011-1340, Gothenburg, Sweden*, 2011. URL https://ntrs.nasa.gov/search.jsp?R=20120000856.

[4] Bradley, M. K., and Droney, C. K., "Subsonic Ultra Green Aircraft Research: Phase 2. Volume 2; Hybrid Electric Design Exploration," NASA Contractor Report, NASA/CR-2015-218704/VOL2, 2015. URL https://ntrs.nasa.gov/search.jsp?R=20150017039&hterms=NASA%2fCR-2015-218704%2fVOL2&qs=N%3D0%26Ntk%3DAll%26Ntt%3DNASA%252FCR-2015-218704%252FVOL2%26Ntx%3Dmode%2520matchallpartial.

[5] Lents, C., Hardin, L., Rheaume, J., and Kohlman, L., "Parallel Hybrid Gas-Electric Geared Turbofan Engine Conceptual Design and Benefits Analysis," *52nd AIAA/SAE/ASEE Joint Propulsion Conference, AIAA Propulsion and Energy Forum, Salt Lake City, UT, AIAA 2016-4610*, 2016. doi:10.2514/6.2016-4610.

[6] Schiltgen, B. T., Freeman, J. L., and Hall, D. W., "Aeropropulsive Interaction and Thermal System Integration within the ECO-150: A Turboelectric Distributed Propulsion Airliner with Conventional Electric Machines," *16th AIAA Aviation Technology, Integration, and Operations Conference, AIAA AVIATION Forum, Washington, D.C., AIAA 2016-4064*, 2016. doi:10.2514/6.2016-4064.

[7] Welstead, J., and Felder, J. L., "Conceptual design of a single-aisle turboelectric commercial transport with fuselage boundary layer ingestion," *54th AIAA Aerospace Sciences Meeting, AIAA SciTech Forum, San Diego, CA, AIAA 2016-1027*, 2016. doi:10.2514/6.2016-1027.

[8] Perullo, C., Trawick, D., Armstrong, M., Tai, J. C., and Mavris, D. N., "Cycle Selection and Sizing of a Single-Aisle Transport with the Electrically Variable Engine(TM) (EVE) for Fleet Level Fuel Optimization," *55th AIAA Aerospace Sciences Meeting, AIAA SciTech Forum, Grapevine, TX, AIAA 2017-1923*, 2017. doi:10.2514/6.2017-1923.

[9] Hahn, S., Park, D. K., Bascuñán, J., and Iwasa, Y., "HTS pancake coils without turn-to-turn insulation," *IEEE Transactions on Applied Superconductivity*, Vol. 21, No. 3, 2011, pp. 1592–1595. doi:10.1109/TASC.2010.2093492.

[10] Song, J.-B., Hahn, S., Lécrevisse, T., Voccio, J., Bascuñán, J., and Iwasa, Y., "Over-current quench test and self-protecting behavior of a 7 T/78 mm multi-width no-insulation REBCO magnet at 4.2 K," *Superconductor Science and Technology*, Vol. 28, No. 11, 2015, p. 114001. doi:10.1088/0953-2048/28/11/114001.

[11] Hahn, S., Radcliff, K., Kim, K., Kim, S., Hu, X., Kim, K., Abraimov, D. V., and Jaroszynski, J., "'Defect-irrelevant' behavior of a no-insulation pancake coil wound with REBCO tapes containing multiple defects," *Superconductor Science and Technology*, Vol. 29, No. 10, 2016, p. 105017. doi:10.1088/0953-2048/29/10/105017.

[12] Umenei, A., Melikhov, Y., and Jiles, D., "Models for extrapolation of magnetization data on magnetic cores to high fields," *IEEE Transactions on Magnetics*, Vol. 47, No. 12, 2011, pp. 4707–4711. doi:10.1109/TMAG.2011.2159616.

[13] Jordan, K., and Stoloff, N., "Plastic deformation and fracture in FeCo–2%V," *Trans. Met. Soc. AIME*, Vol. 245, 1969, pp. 2027–34.